Simulated Convective Lines with Leading Precipitation. Part II: Evolution and Maintenance

MATTHEW D. PARKER* AND RICHARD H. JOHNSON

Department of Atmospheric Science, Colorado State University, Fort Collins, Colorado

(Manuscript received 7 April 2003, in final form 2 February 2004)

ABSTRACT

This article, the second of two describing a study in which the authors used idealized numerical simulations to investigate front-fed convective lines with leading stratiform precipitation (FFLS systems), addresses the dynamics and sensitivities governing the systems' evolution toward other structures and their sustenance despite the apparent contamination of their inflow by preline precipitation. Sensitivity tests show that the middle- and upper-tropospheric wind shear are important to the updraft tilt and overall structure of the simulated systems. In time, simulated FFLS systems tend to evolve toward a convective line with trailing stratiform (TS) precipitation structure because they tend to decrease the line-perpendicular vertical wind shear nearby. This, along with gradual increases in the system's cold pool strength, contributes to more rearward-sloping updrafts and may initiate a positive feedback mechanism that hastens transition toward TS structure. However, whereas the system's tendency to decrease the local shear favors the demise of the FFLS mode, the presence of precipitation on its line-leading side actually favors its maintenance. FFLS systems are able to destabilize their own inflow in the preline precipitation region owing to the vertical profile of evaporation and melting and to lifting, a feature that is quite robust in the simulations. The authors conclude this second article with a general restatement of FFLS dynamics based upon synthesized results from the pair of papers.

1. Introduction

Convective lines with leading stratiform (LS) precipitation are common in the central United States (Parker and Johnson 2000, hereafter PJ00) and yet they have received comparatively little study among the various archetypes for mesoscale convective systems (MCSs). This paper is the second of two addressing the basic structures of *front-fed LS (FFLS) systems*, and the dynamics that account for and sustain them; the companion paper, Parker and Johnson (2004a), is hereafter referred to as ''Part I.'' In Part I, the authors set the problems associated with FFLS systems and cast them within the long lineage of observational and numerical papers about MCSs. The authors then focused on simulated FFLS systems' quasi-stable long-lived structures and on the dynamics that govern their updrafts and downdrafts. Foremost among the findings in Part I are that the accelerations causing inflowing air parcels to ascend and overturn in deep convective updrafts (and thereby produce line-leading precipitation) are transient, and are attributable to a combination of the horizontal gradients in the buoyant, linear dynamic, and nonlinear dynamic pressure fields. Precipitation, which falls into the inflowing airstream in the preline region, appears to govern the period of the FFLS multicell system; for each updraft cycle there is a point of cutoff when inflowing air parcels experience downward accelerations owing to hydrometeor loading as they approach the updraft.

The present paper (Part II) focuses on a mechanism that enables the simulated FFLS systems to survive for multiple hours the intuitively detrimental effects of preline precipititation upon their inflow, mechanisms by which an FFLS system evolves toward an FFTS [front-fed convective line with trailing stratiform (TS) precipitation] structure in time, and the modeled sensitivities governing these processes. Of note in this regard are numerous prior numerical sensitivity studies for squall lines, including those by Hane (1973), Thorpe et al. (1982), Seitter and Kuo (1983), Dudhia et al. (1987), Nicholls et al. (1988), Weisman et al. (1988), and Szeto and Cho (1994). Alongside the former, the present simulations stand to fill yet a bit more of the vast thermodynamic and kinematic phase space in which convective systems may occur. In particular, this article addresses some of the primary results of Weisman et al. (1988, along with Rotunno et al. 1988), as they concern the sensitivities of FFLS systems.

In the following section we briefly describe the meth-

* Current affiliation: Department of Geosciences, University of Nebraska at Lincoln, Lincoln, Nebraska.

Corresponding author address: Dr. Matthew Parker, 214 Bessey Hall, University of Nebraska at Lincoln, Lincoln, NE 68588-0340.
E-mail: mparker@papagayo.unl.edu

ods used in this paper as they differ from Part I. Section 3 discusses the evolution and demise of FFLS structure in the idealized simulations, and the sensitivities that shed light on this process. Section 4 describes the maintenance of FFLS systems despite preline precipitation, and the sensitivities of this mechanism to the model's microphysical scheme. Thereafter, we present a consolidated view of FFLS systems' structures, dynamics, and behaviors, representing a synthesis of the results from both Parts I and II. Finally, the paper concludes with some ideas for future work and a brief summary.

2. Methods

Just as in Part I, this paper makes use of idealized numerical simulations with the Advanced Regional Prediction System [ARPS; Xue et al. (1995, 2000, 2001)] in order to describe the basic evolutions and dynamics of front-fed convective lines with leading precipitation. Except as noted in this section, the configuration of the numerical model and methods of analysis are identical to those described in Part I.

a. Basic sensitivities

In order to test the sensitivity of the quasi-stable FFLS system and its evolution to the wind profile and to the local vorticity balance theory suggested by Rotunno et al. (1988), we varied both the vertical profile of the *u* wind and the evaporation rate in the model. The base-state wind profile for the control simulations is shown in Fig. 1. This is identical to the wind profile shown by the barbs in Fig. 3 of Part I. In Part II, we refer to this control profile as "$S=16$", because the 3–10-km vector wind difference was $\sim$16 m s^{-1}. The two variations shown in Fig. 1 are called "$S=10$" and "$S=4$", because they are identical to the control sounding below 3 km AGL, but, respectively, have 3–10-km vector wind differences of $\sim$10 and 4 m s^{-1}.

Additionally, for the purposes of sensitivity studies, it was useful to modify the strength (density perturbation) of the surface pool of cold outflow. Therefore, additional tests included simulations whose environmental profiles of temperature, humidity, and wind were identical to the control sounding (Fig. 3 of Part I), but whose cold pools were different from one another because of the different evaporative chilling rates. This isolated the effects of evaporative chilling and the cold pool's strength on the systems' evolution without fundamentally altering the storms' initial structures and basic processes. The sensitivity studies were simple modifications of the model's rain evaporation rate by a multiplicative factor. The control simulation is referred to as "$E=1$" (evaporation rate unmodified); the two sensitivity tests are referred to as "$E=0.5$" (evaporation rate halved) and "$E=2$" (evaporation rate doubled).

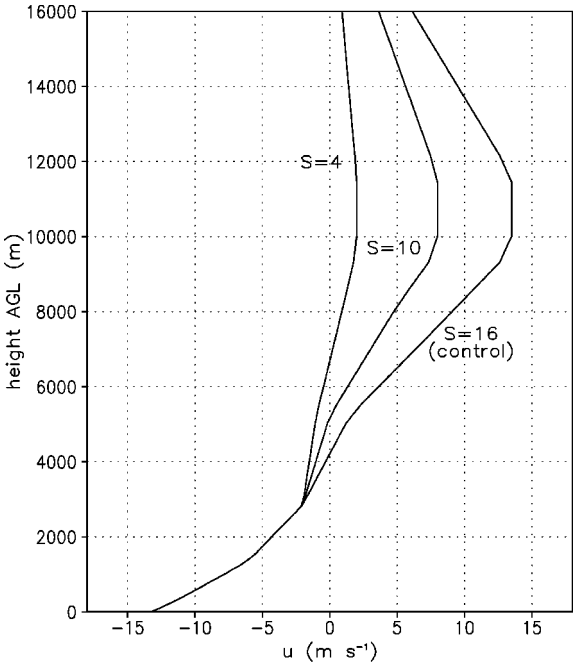

FIG. 1. Profiles of *u* wind used in this study. The mean front-fed LS MCS wind profile is labeled as $S=16$ (3–10-km vector wind difference $\approx$ 16 m s^{-1}); $S=10$ and $S=4$ are modified wind profiles with decreased wind shear above 3 km AGL (3–10-km vector wind differences $\approx$10 and 4 m s^{-1}, respectively).

b. Sensitivities to microphysical parameters

It will be shown in section 4 that the longevity of FFLS systems is partly attributable to destabilization of inflowing air. This destabilization is strongly related to both the horizontal shape of the leading precipitation region and to local chilling from the melting of graupel. Therefore, we also performed several sensitivity tests with the model microphysics packages, in order to determine the robustness of the process. First, in addition to the control run, which utilized the Lin et al. (1983) ice microphysics scheme, we performed additional simulations using identical model configurations except that in one case we used the ARPS ice microphysics package based on that designed by Schultz (1995), and in the other we used the ARPS liquid-only microphysics package based on that designed by Kessler (1969). Additionally, in order to assess the sensitivity of the destabilization mechanism to the graupel phase, we modified basic parameters describing the inverse-exponential size distribution in the Lin et al. (1983) ice microphysics scheme:

$$n_g(D) = n_{og} \exp(-D\lambda_g), \tag{1}$$

wherein the number of particles n_g is a function of diameter D, the intercept parameter n_{og}, and the slope paremeter λ_g. In turn, the slope parameter of the distribution λ_g is determined via

TABLE 1. Parameter settings for sensitivity tests to the graupel particle size distribution: ρ_g, the graupel density (g cm^{-3}), and n_{og}, the graupel distribution's intercept parameter (cm^{-4}).

Run name	ρ_g (g cm^{-3})	n_{og} (cm^{-4})
Control	0.9	4×10^{-4}
$\rho 4$	0.4	4×10^{-4}
$n10^{-3}$	0.9	4×10^{-3}
$n10^{-5}$	0.9	4×10^{-5}

$$\lambda_g = \left(\frac{\pi \rho_g n_{og}}{\rho_a q_g}\right)^{0.25}, \tag{2}$$

wherein ρ_a and ρ_g are the densities of air and graupel, respectively, and q_g is the graupel mixing ratio. In the present study, we modified ρ_g and n_{og}, whose values have been shown to vary in nature and to which the graupel size distribution and mean fall speeds are quite sensitive. The magnitudes of these modifications were based upon the discussion presented by Gilmore et al. (2002), and are summarized in Table 1.

c. Reintroduction of abbreviations

As in Part I, this paper describes the buoyant (p'_B), dynamic linear (p'_{DL}), and dynamic nonlinear (p'_{DNL}), pressure perturbations, which are defined via

$$\nabla^2 p'_B = \frac{\partial}{\partial z}(\rho_o B); \tag{3}$$

$$\nabla^2 p'_D = -\rho_o\left[\left(\frac{\partial u}{\partial x}\right)^2 + \left(\frac{\partial v}{\partial y}\right)^2 + \left(\frac{\partial w}{\partial z}\right)^2 - w^2\frac{\partial^2}{\partial z^2}(\ln\rho_o)\right] - 2\rho_o\left(\frac{\partial v}{\partial x}\frac{\partial u}{\partial y} + \frac{\partial u}{\partial z}\frac{\partial w}{\partial x} + \frac{\partial v}{\partial z}\frac{\partial w}{\partial y}\right); \tag{4}$$

$$\nabla^2 p'_{DL} = -2\rho_o\frac{du_o}{dz}\frac{\partial w}{\partial x}; \tag{5}$$

$$p'_{DNL} = p'_D - p'_{DL}. \tag{6}$$

The paper also incorporates abbreviations for the accelerations associated with the above pressure perturbations as follows:

$$\underbrace{\frac{D\mathbf{u}}{Dt}}_{\text{ACC}} = \underbrace{\underbrace{-\frac{1}{\rho_o}\nabla p'_B}_{\text{ACCB}} \underbrace{-\mathbf{g}\left(\frac{\rho'_{\text{gas}}}{\rho_o}\right)}_{\text{BUOY}} \underbrace{-\mathbf{g}q_h}_{\text{DRAG}} \underbrace{-\frac{1}{\rho_o}\nabla p'_{DL}}_{\text{ACCDL}} \underbrace{-\frac{1}{\rho_o}\nabla p'_{DNL}}_{\text{ACCDNL}}}. \tag{7}$$

These terms are described in more detail in Part I.

3. FFLS systems' evolution toward FFTS structure

a. Basic system evolution

Much as was mentioned by Parker and Johnson (2004b), almost all of the simulated 2D FFLS systems (and the periodic-3D systems in weaker deep-layer shear) eventually evolve toward a FFTS structure. Understanding the physical causes for this transformation is important to the short-term predictability of MCSs' organizational modes. As noted in Part I, FFLS systems appear to be somewhat unique in that they significantly decrease the low-level environmental shear in their preline regions. Following the work of Rotunno et al. (1988), and as discussed for various quasi-2D convective modes by Parker and Johnson (2004b), this decrease in shear should favor more rearward storm-relative velocities for air parcels that are processed by the convective region. Such a condition should therefore be consistent with a tendency toward the FFTS structure, as inflowing air parcels increasingly carry water rearward from the convective region. In this section, we discuss physical processes that appear to play key roles in the evolution of the control 2D FFLS simulation toward FFTS structure from roughly $t = 4$ h onward (Fig. 2a, and Fig. 5 in Part I).

As discussed in Part I, many of the updrafts in the 2D FFLS simulations do not penetrate into the middle and upper troposphere until they are well aft (on the order of 10 km rearward) of the surface outflow boundary (e.g., parcel △ in Fig. 15 of Part I). This is largely related to the negative buoyancy contributed by evaporation and water loading due to the line-leading precipitation in the convective region. One example of this, around $t = 3.9$–4.1 h (Fig. 2c), occurs after roughly 30 min of suppression, in which the only updraft (around $t = 3.75$ h) was considerably weaker than its predecessors. Although it is difficult to state exactly why the new cell around $t = 4$ h is much stronger than most of the prior updrafts in the simulation, it appears to be partly related to the comparatively smaller hydrometeor load in the convective region during its formation (the channel of minimized reflectivity moving rearward between $t = 3.6$ and 4 h in Fig. 2a). This strong cell around $t = 4$ h heralds the onset of a change in the convective system's behavior.

In particular, between $t = 4$ and $t = 4.5$ h, two new updrafts are subsequently initiated, each one closer to the surface outflow boundary than its predecessor (Fig. 2c). Although it is difficult to infer from Fig. 2b, animated cross sections reveal that as each strong cell reinforces the surface outflow, the cold pool is significantly deepened immediately below the precipitation core. This hastens the development and vertical penetration of the next updraft in the sequence, which is initiated on the forward-facing side of the new hump in the cold pool, aft of the surface outflow boundary but farther forward than the preceding cell. This feedback occurs three times, until at $t = 4.75$ h, the updrafts are nearly centered above the surface outflow boundary (Fig. 2c). In addition to the fact that this behavior corresponds to the production of heavy precipitation progressively farther forward within the system (Fig. 2a),

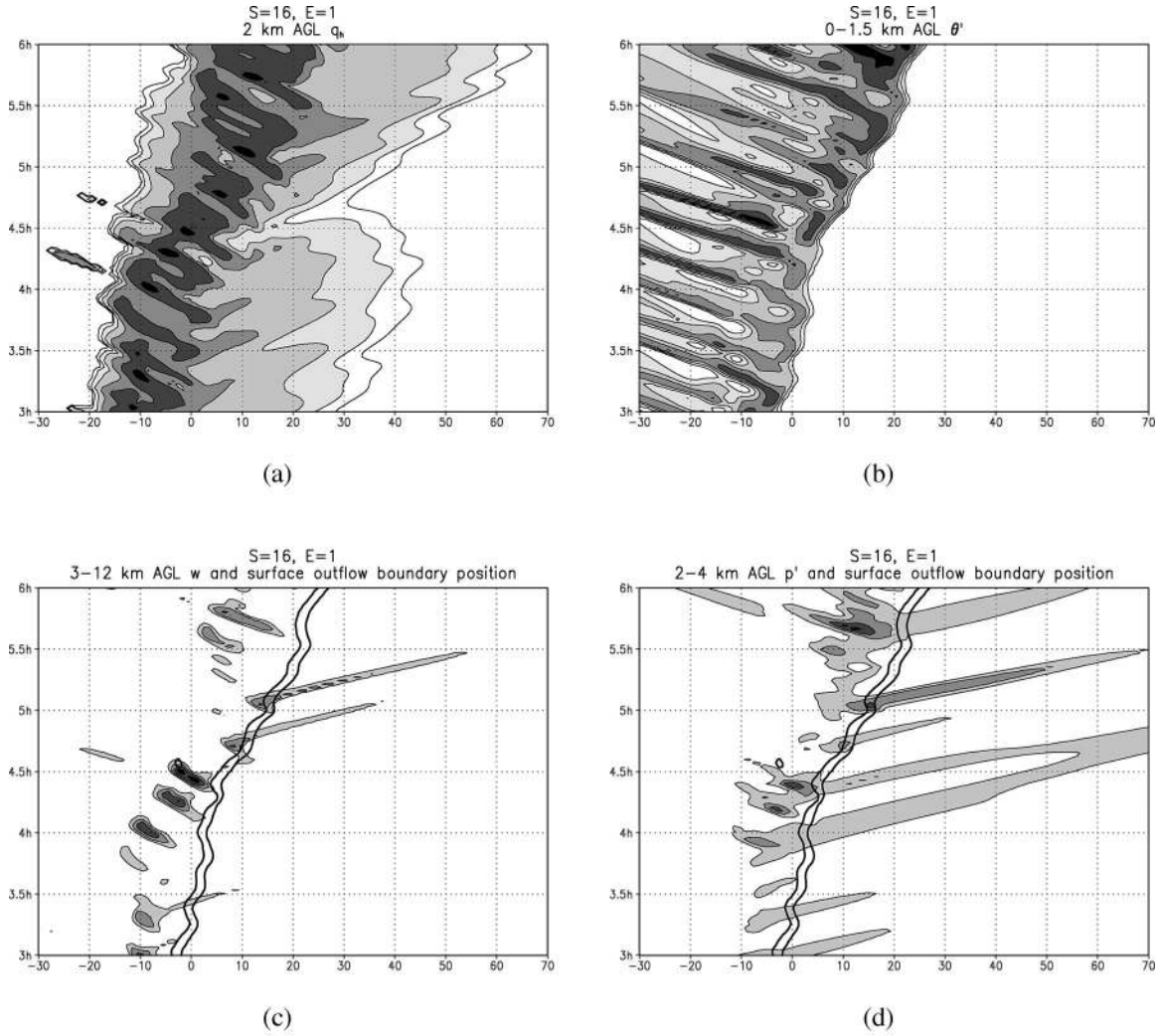

FIG. 2. Hovmöller diagrams (from $t = 3$–6 h) for $S=16$, $E=1$ (control) simulation depicting (a) 2-km-AGL hydrometeor mixing ratio (levels of shading are 0.005, 0.02, 0.08, 0.32, 1.28, and 5.12 g kg^{-1}), (b) 0–1.5-km-AGL mean θ' (levels of shading are -2, -3.5, -5, -6.5, and -8 K), (c) 3–12-km-AGL mean w (levels of shading are 4, 8, 12, and 16 m s^{-1}), and (d) 2–4-km-AGL mean p' (levels of shading are -2, -3, -4, and -5 hPa). In (c) and (d), the position of the surface outflow boundary is shown by a heavy contour of $\partial\theta/\partial x = 0.002$ K m^{-1}.

this progression of strong updrafts also has longer-term effects on the system's organizational mode.

First, the three strong updrafts in rapid succession contribute a great deal of evaporatively chilled air to the surface cold pool, in addition to which the weight of their suspended hydrometeors also hydrostatically intensifies the surface pressure maximum in the cold pool. As well, because each successive cell occurs in increasing proximity to the surface outflow boundary, the progression of updrafts delivers a large quantity of cold air just aft of the surface gust front in a very short amount of time. By $t = 4.4$ h, the decrease in the cold pool's temperature is evident in close proximity to the outflow boundary (Fig. 2b). As a result, around $t = 4.4$ h, the outflow boundary's speed increases dramatically; indeed, this is the single largest acceleration of the outflow speed during the entire 8 h of the control simulation. The system does not stop producing leading precipitation immediately. However, with time the horizontal gradient in q_h decreases on the system's trailing edge and increases on its leading edge. These are symptoms that fewer updraft parcels are carrying water forward from the convective line and more are carrying water rearward and contributing to a trailing precipitation region. This behavior also occurred in our other simulations, and the transition in most of those simulations was quite similar.

The increasingly rearward final velocities of the updraft parcels are attributable to several processes. Most straightforward is that, as the system speed increases, all parcels have greater rearward components to their storm-relative velocities. Second, as the surface cold

pool strengthens, it tends to produce greater rearward accelerations upon the air parcels that it has lifted. As explained by Rotunno et al. (1988), and diagnosed for various quasi-2D MCSs by Parker and Johnson (2004b), this effect can produce rearward-canted updrafts. This is especially significant for mature FFLS systems because they decrease the lower-tropospheric wind shear (as discussed in Part I and shown there in Fig. 12), which in turn diminishes the downshear contributions of ACCDL in the lower troposphere. Hence, updraft parcels in time possess greater rearward storm-relative velocities owing to smaller rear-to-fore accelerations and greater system speed, and the updrafts thereby acquire more rearward tilt.

Notably, coincident with the evolution of the FFLS system toward FFTS structure, the pressure in the lower-to-middle troposphere decreases just behind the convective line (Fig. 2d). Szeto and Cho (1994) found in their simulations that a meso-γ (Orlanski 1975) pressure minimum, occurring just to the rear of convective lines owing to both buoyant and dynamic contributions, was central to the rapid evolution of a fairly upright convective line into a well-developed TS system. This low pressure center initiated a positive feedback mechanism, whereby inflowing air was accelerated rearward toward the pressure minimum, which rendered a more rearward tilt to the updraft trajectories, which in turn tended to reinforce the pressure minimum both thermally and dynamically. Szeto and Cho (1994) did not dispute the significance of the cold pool to system evolution; rather, they stated that ''. . .the intensification of the cold pool is partly due to the upshear development of the system. . .'' It is difficult to determine the degree to which this 2–4-km-AGL pressure minimum, which continues to deepen unsteadily in time (through $t = 6$ h, Fig. 2d and onward), is a symptom of the increasing rearward tilt as opposed to an active player. Nevertheless, its presence and increasing strength do render larger rearward pressure gradient accelerations for air parcels in the updraft region, thereby reinforcing the developing TS structure.

The system structure and dynamics following the LS–TS transition (cross section in Fig. 3) are dramatically different from those of the quasi-stable FFLS phase of the system (before $t = 4$ h, as discussed at length in Part I). For example, at $t = 7$ h 35 min, the pressure field is far more perturbed (Fig. 4b; cf. Fig. 16 from Part I), the convective updraft is far less erect (Fig. 4a), and the cold pool is somewhat stronger (Fig. 4a). Much as was diagnosed by Szeto and Cho (1994), the pressure minimum to the rear of the primary convective cell has significant contributions from both p'_B and p'_D (specifically, p'_{DNL}). Above approximately 5 km AGL in the updraft, the net ACC remains downshear (Fig. 4b). However, Fig. 4a reveals that most of the air in the updraft is not ascending very far above 5 km AGL because the updraft comprises air parcels with very large rearward velocities (in places, $u < -30$ m s^{-1}). Additionally, the net ACC vectors are nearly horizontal above 5 km AGL owing to the strong downward ACCDNL, such that air parcels ascending above 5 km do not gain any additional vertical momentum. As a result of these effects, inflowing air parcels move through the upward forcing very quickly and then proceed rearward within a plume of quasi-horizontal flow (i.e., at $x = 26$ to $x = 33$ km, $z = 3$ to $z = 7$ km AGL in Fig. 4a).

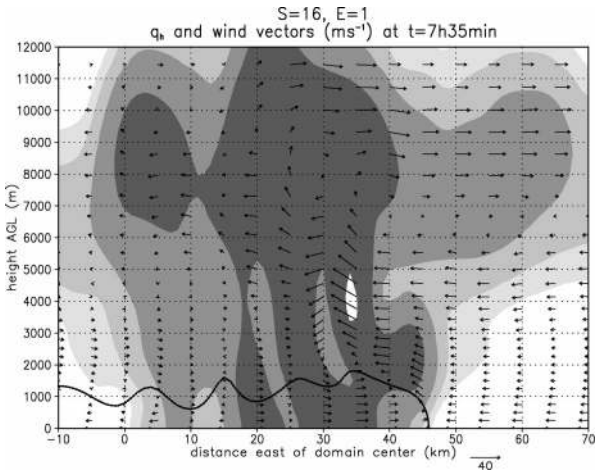

FIG. 3. Total hydrometeor mixing ratio (levels of shading are 0.02, 0.08, 0.32, 1.28, and 5.12 g kg^{-1}) and wind vectors (m s^{-1}, scaled as shown) for the $S=16$, $E=1$ (control) simulation at $t = 7$ h 35 min. The $\theta' = -4.5$ K isopleth is also plotted to show the cold pool's position.

As has been mentioned, nearly every 2D FFLS simulation eventually evolved toward TS structure. This suggests that, although the parameter space in which 2D FFLS systems can occur is fairly broad, the parameter space in which an FFLS system can be indefinitely long lived (like its FFTS cousin) is quite small. This has implications for the mean MCS lifetimes reported by PJ00, who found that LS systems were much shorter-lived than TS systems on average. Because PJ00 classified systems based upon their predominant organizational modes, they classified as TS any long-lived systems that had significant LS phases but evolved toward and persisted with TS structure for longer periods of time. The present study suggests that this transition is common and dynamically favored. PJ00 found that 30% of the LS systems that they studied evolved into TS systems while 65% remained with LS structures until they decayed. This may mean that the relatively short mean lifetimes for LS systems reported by PJ00 were symptoms that most of the longer-lived systems in their population evolved into a TS structure, and hence were not classified as LS in their study.

Notably, however, the 3D FFLS simulations in the present study were much more robust; only in experiments with considerably weaker deep-layer wind shear did the periodic-3D systems evolve toward TS structure within the first 6–10 h of simulation, and the 3D ex-

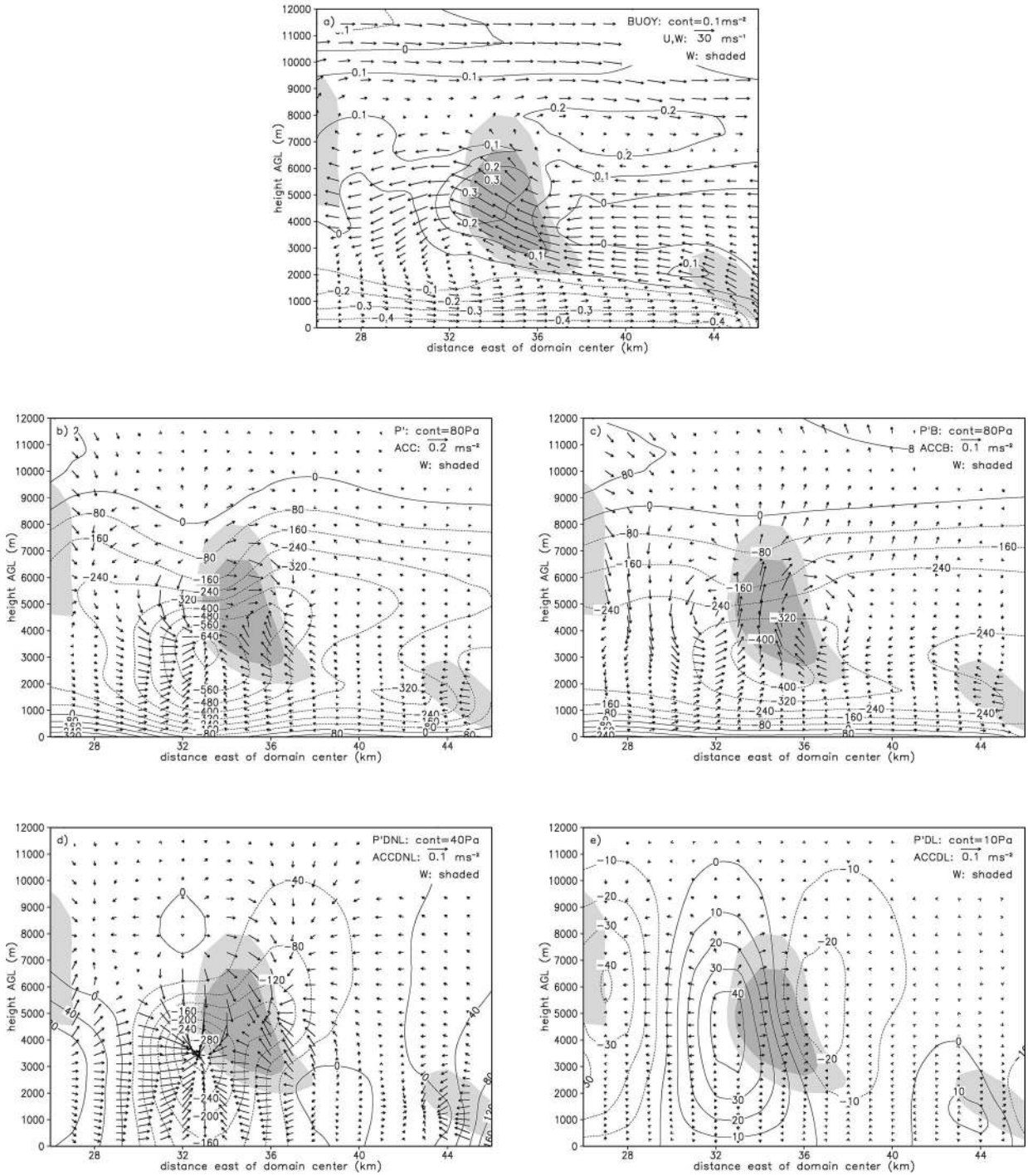

FIG. 4. Velocities, perturbation pressures, and acceleration terms for simulation $S=16$, $E=1$ (control) at 7 h 35 min. (a) BUOY contoured, u and w vectors; (b) p' contoured, ACC vectors; (c) p'_B contoured, ACCB vectors; (d) p'_{DNL} contoured, ACCDNL vectors; (e) p'_{DL} contoured, ACCDL vectors. Vertical velocity shaded in all panels: levels of shading are 5 and 10 m s^{-1}. Contour intervals and vector scales are shown for each panel, and vary among panels. Terms are defined in section 2c.

periment using open along-line boundary conditions also retained FFLS structure through 6 h. If the foregoing discussion accurately describes the LS–TS transition, the greater resistance of 3D systems to this process is attributable to the generally smaller hydrometeor loads and pressure perturbations that are associated with the mature 3D structures. As discussed in Part I, 3D systems produce less total condensate. Therefore, they

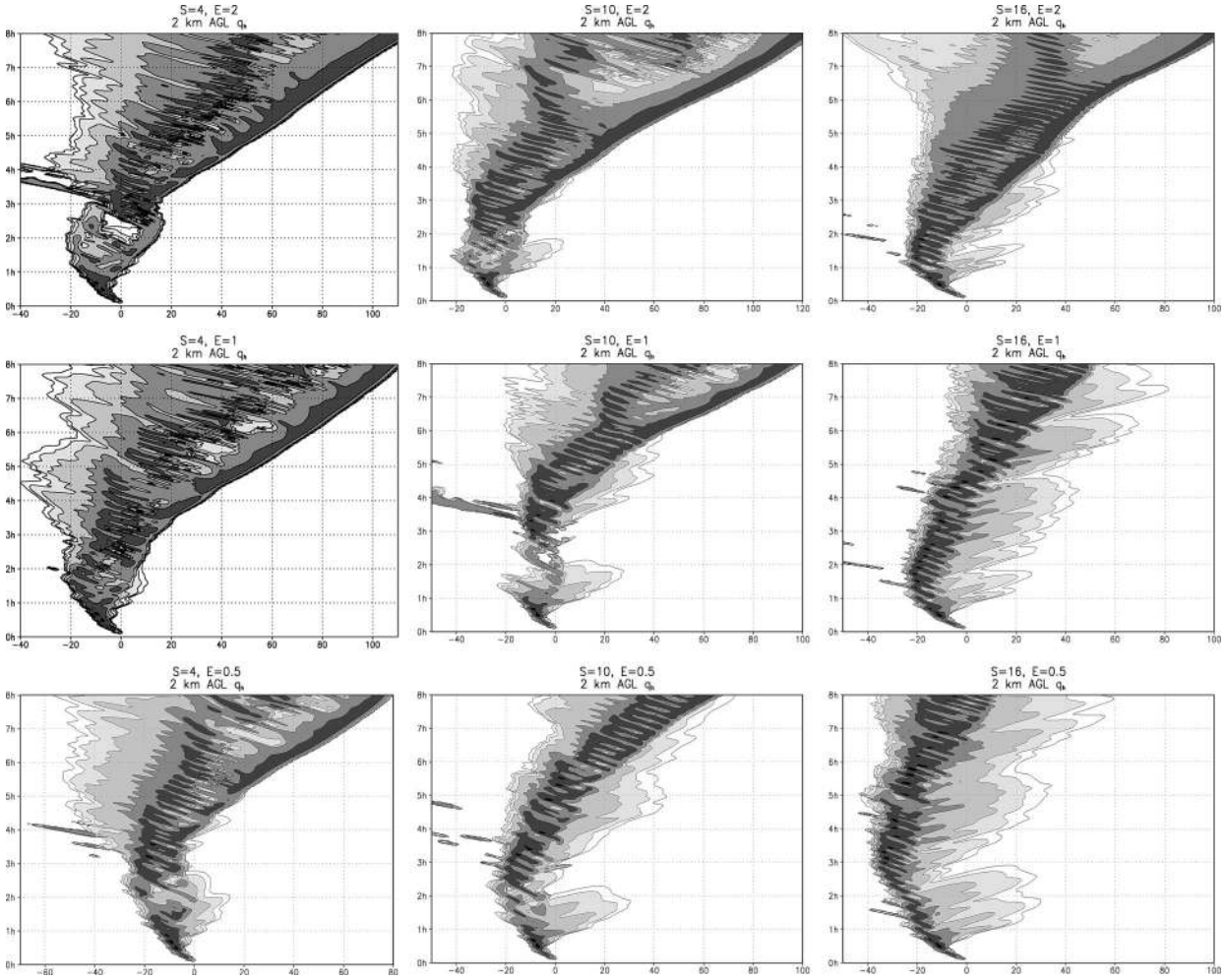

FIG. 5. Matrix of Hovmöller diagrams depicting 2-km-AGL hydrometeor mixing ratio (t = 0–8 h) for 3–10-km shear (S) = 4, 10, 16, and evaporation rate factor (E) = 0.5, 1, 2. Levels of shading are 0.005, 0.02, 0.08, 0.32, 1.28, and 5.12 g kg^{-1}. The front-fed LS control run is S=16, E=1.

produce weaker surface cold pools and weaker midlevel preline pressure minima, as a result of which they do not increase the vertical shear in their preline regions as dramatically as 2D systems (Part I). As well, the 3D updrafts tend to be more erect (Part I), and therefore may be more resistant to any positive feedbacks associated with the Szeto and Cho (1994) line-trailing low mechanism. Until more detailed case studies can be performed, it will remain unclear to what degree real-world FFLS systems resemble the fully 3D simulations as opposed to the 2D results. Reflectivity data for the FFLS systems studied by PJ00 (e.g. their Fig. 6) did reveal individual cells along the systems' convective lines which, in a moderate to high shear regime, can imply a fairly large degree of local three-dimensionality.

b. Related sensitivities

This section discusses several sensitivity tests whose purpose is to help elucidate the dynamics of the simulated FFLS systems. Although this may, in part, overlap with some previous studies (e.g., Hane 1973; Thorpe et al. 1982; Dudhia et al. 1987; Nicholls et al. 1988; Weisman et al. 1988; Szeto and Cho 1994), the results are included here in order to show the robustness of the FFLS structure and the basic effects of variations to the typical FFLS environment; they are not meant to demonstrate the full breadth of convective modes that are possible. As overviewed by Parker and Johnson (2004b), although a surface cold pool's strength with respect to the lower-tropospheric environmental shear is indeed relevant to quasi-2D MCS dynamics (Rotunno et al. 1988), the wind profile in the 3–10-km-AGL layer is also important. A matrix of nine 2D simulations used the three wind profiles shown in Fig. 1 (S=16, S=10, and S=4) along with three multiplicative factors (E=2, E=1, and E=0.5) for the evaporation rate. The resulting system structures are shown via Hovmöller diagrams in Fig. 5.

All of the simulated systems initially produced down-

TABLE 2. Mean integrated rearward accelerations, expressed as the mean Δu (m s^{-1}) between parcels' initial and most rearward velocities, along updraft trajectories in each of the nine shear/evaporation experiments.

	$S=4$	$S=10$	$S=16$
$E=2$	−8.2	−10.9	−7.9
$E=1$	−7.5	−4.5	−2.1
$E=0.5$	−5.3	−4.5	−1.9

TABLE 3. Mean integrated forward accelerations, expressed as the mean Δu (m s^{-1}) between parcels' most rearward and updraft-departing velocities, along updraft trajectories in each of the nine shear/evaporation experiments.

	$S=4$	$S=10$	$S=16$
$E=2$	9.4	22.5	29.0
$E=1$	10.3	19.4	21.7
$E=0.5$	9.9	18.5	22.0

shear-tilted updrafts and leading precipitation. And, with the exception of the simulation with the strongest shear and lowest evaporation rate ($S=16$, $E=0.5$), all of the simulated systems eventually evolved from their initial FFLS structure into a FFTS structure (Fig. 5). Not surprisingly, given the basic dynamics discussed in the first part of this section, simulated systems in stronger deep-layer wind shear maintained their leading precipitation regions longer (in Fig. 5, deep-layer shear increases from left to right), and simulated systems with larger evaporation rates evolved toward TS structure more rapidly (in Fig. 5, evaporation rate increases from bottom to top). Because the lower-tropospheric wind profile was not varied in these experiments, it seems clear that the determination of LS versus TS system structure is more complicated than what Rotunno et al. (1988) envisioned. The simulated structures are nicely stratified by the 3–10-km wind shear: for the $E=0.5$ simulations, $S=16$ produced a long-lived FFLS structure, $S=4$ produced a long-lived FFTS system, and $S=10$ produced a hybrid.

Although it is not feasible to individually analyze and compare large numbers of individual trajectories from these simulations, it is possible to extract the mean behaviors of groups of trajectories. Following Part I, the important accelerations within convective systems are lost in simple temporal averages; therefore, the analysis in this section averages numerous trajectories that individually ascended in updrafts and experienced these transient accelerations. Each simulation included 1000 air parcels, launched into the lowest 2 km of the inflowing airstream, spaced such that they arrived at the convective region regularly throughout the systems' mature periods. In each case, between 220 and 455 of the parcels ascended in a convective updraft. Tables 2–6 together summarize the overall behavior of the updraft air parcels from the nine experiments. For each simulation, mean u velocities along the updraft parcels' trajectories reveal the character of the net front-to-rear and rear-to-front accelerations. Table 2 (discussed in more detail later) represents the mean change in u between updraft parcels' initial and most rearward velocities; Table 3 (discussed in more detail later) then represents the mean change in u between the parcels' most rearward velocities and their velocities as they leave the updraft. Because most of the updraft trajectories attained their maximum rearward velocities near 3 km AGL, this kind of separation nicely isolates the role of the 3–10-km wind shear magnitude.

All of the simulations began with identical wind profiles below 3 km AGL. Therefore, for all nine simulations, the mean initial u velocities of the updraft parcels were about the same, roughly -7 m s^{-1} (± 0.7 m s^{-1}). The mean rearward parcel accelerations were primarily sensitive to the evaporation rate, with increasing net rearward accelerations for higher evaporation rates (from bottom to top in Table 2). The reason for this relationship is that greater evaporation rates render stronger surface cold pools, which in turn imply greater rearward ACCB and ACCDNL, as described in Part I. There was also a weak tendency for the mean rearward accelerations to be larger for smaller values of the 3–10-km shear vector (from right to left in Table 2). It is more difficult to assess the dynamics of this relationship because, as previously mentioned, the rearward accelerations occur almost entirely below 3 km AGL. Because the updraft trajectories in the $S=4$ simulations do not strongly overturn, rearward-tilted systems occur, which drop most of their precipitation on the same side of the gust front as the preexisting cold pool, whereas FFLS systems in the $S=16$ simulations drop a significant fraction of their precipitation on the leading side of the gust front, away from the preexisting surface cold pool. As a result of these factors, in the $E=0.5$–1 experiments, the $S=16$ systems are far less effective at reinforcing their own cold pools than are the $S=4$ systems; this, in turn, somewhat weakens the ACCB and ACCDNL associated with the outflow.

On average, once the air parcels reach 3 km AGL, they have attained their maximum rearward velocities and are ascending into a region of rear-to-front acceleration. As should be expected based on the discussions in Part I, even though there is a very weak sensitivity to the evaporation rate, the greatest tendency is for the net rear-to-front acceleration of the updraft parcels to grow with increasing 3–10-km shear magnitude (from left to right in Table 3). The large sensitivity to the 3–10-km wind shear is due to the importance of the base-state wind shear to p'_{DL} and ACCDL, as well as the feedbacks through ACCB and ACCDNL, which often also help to contribute in the direction toward which ACCDL causes the cloud to tilt (as in Part I). The weak tendency for larger forward accelerations with increased evaporation rate (from bottom to top in Table 3) apparently exists because stronger surface cold pools tend to produce marginally stronger updrafts, and p'_{DL} in turn is also a function of the horizontal gradient in w within

TABLE 4. Mean final u velocities (m s^{-1}) of updraft parcels in each of the nine shear/evaporation experiments.

	S=4	S=10	S=16
E=2	−5.6	4.6	13.3
E=1	−4.4	6.2	13.4
E=0.5	−3.2	6.6	14.3

TABLE 5. Mean gust front translational speeds (m s^{-1}) in each of the nine shear/evaporation experiments.

	S=4	S=10	S=16
E=2	3.2	3.2	5.8
E=1	3.4	1.1	3.9
E=0.5	0.9	0.7	2.0

the updraft (i.e., for a given updraft width, $p'_{DL}$is a function of the updraft's strength). Although the lower-tropospheric rearward accelerations are sensitive to the evaporation rate, the upper-tropospheric forward accelerations are even more strongly sensitive to the 3–10-km wind shear. As a result, the mean final u velocities of the updraft parcels in the nine simulations were grouped almost entirely based on the deep-layer shear, and increased significantly for larger values of S (from left to right in Table 4). The distribution of integrated accelerations (i.e., the initial velocities ≈ -7 m s^{-1}, subtracted from Table 4) was broad, ranging from +2.8 m s^{-1} for the S=4 cases to +20.8 m s^{-1} for the S=16 cases. The importance of the upper-tropospheric shear in these experiments is consistent with Grady and Verlinde's (1997) interpretation of a well-observed case with FFLS characteristics.

The preceding analysis suggests that the cold pool's strength is less relevant to the updraft parcel accelerations than is the deep-layer shear. However, because surface outflow behaves roughly like a density current (Charba 1974), its speed is proportional to its depth and temperature perturbation. Therefore, in the matrix of nine simulations, the system's eastward speeds increased with increasing evaporation rate (from bottom to top in Table 5). From this perspective, the cold pool strength is important because it determines the system speed, which in turn determines the final storm-relative velocities for air parcels with a given ground-relative u velocity. As a result, the final mean storm-relative line-perpendicular parcel velocities are sensitive to both the evaporation rate and the 3–10-km-AGL wind shear (Table 6). In cases with large E and small 3–10-km shear (upper left of Table 6), parcels on average departed the updrafts with significant front-to-rear momentum; in cases with small E and large 3–10-km shear (lower right of Table 6), parcels on average departed the updrafts with significant rear-to-front momentum. Part I argued that the mean final storm-relative u of individual air parcels contributes to the development of either a leading or trailing precipitation region, and the data from Table 6 and Fig. 5 bear this out. Notably, the system speeds given in Table 5 are averages over the entire 8 h of each simulation; most of the systems accelerated later in their lifetimes, which is consistent with increasingly rearward storm-relative parcel velocities and hence the systems' evolutions from LS toward TS structure.

Similar sensitivity tests in the periodic-3D simulations provided comparable results, with the caveat that they were generally less sensitive to the aforementioned changes in S and E. Analyses suggest that this is largely because the 3D system perturb their environment to a smaller degree and in a temporally smooth way, thereby dampening the mechanisms that cause a FFLS–FFTS transition, as in the first part of this section. Notably, if the deep-layer shear is increased beyond S=16, uniquely 3D quasi-supercellular elements begin to develop. An example of this is shown in Fig. 6b for a simulation with S=22 (3–10-km vector wind difference ≈22 m s^{-1}; profile not shown, but can be inferred from Fig. 1). Cells along the S=22 FFLS system's line are slightly more intense and isolated than those in the S=16 simulation (cf. Figs. 6a,b), and the domain-averaged unsigned vorticity ($|\zeta|$) at 5 km AGL is nearly twice that of the control simulation (not shown). This suggests that FFLS systems lie in the spectrum between the FFTS and supercellular modes, and represent the high-shear limit of the quasi-2D regime.

4. Maintenance

a. Destabilizing effect of preline precipitation

As described in Part I, front-fed systems with leading precipitation can be long lived and *quasi stable*. PJ00 noted that: ''a fundamental question. . . regarding the longevity of LS cases [is] their persistence despite inflow of evaporatively cooled preline air into convective towers.'' If an inflow layer is relatively shallow, evaporation of precipitation falling into that layer would cool its air parcels, thereby adding convective inhibition (CIN) with respect to the original sounding. However, an important result of the present study is that, because front-to-rear storm-relative inflow occurs over a relatively deep layer,[1] cooling also occurs over a relatively deep layer and this destabilizes the near-line sounding for most of the system's mature phase. As shown in Fig.

[1] The front-to-rear inflow layer is nearly 6 km deep in the present study. It was about 5.5 km deep in the mean profile presented by *PJ*00, as can be inferred from their Fig. 12.

TABLE 6. Mean final storm-relative u velocities (m s^{-1}) of updraft parcels in each of the nine shear/evaporation experiments.

	S=4	S=10	S=16
E=2	−8.8	1.4	7.5
E=1	−7.8	5.1	9.5
E=0.5	−4.1	5.9	12.3

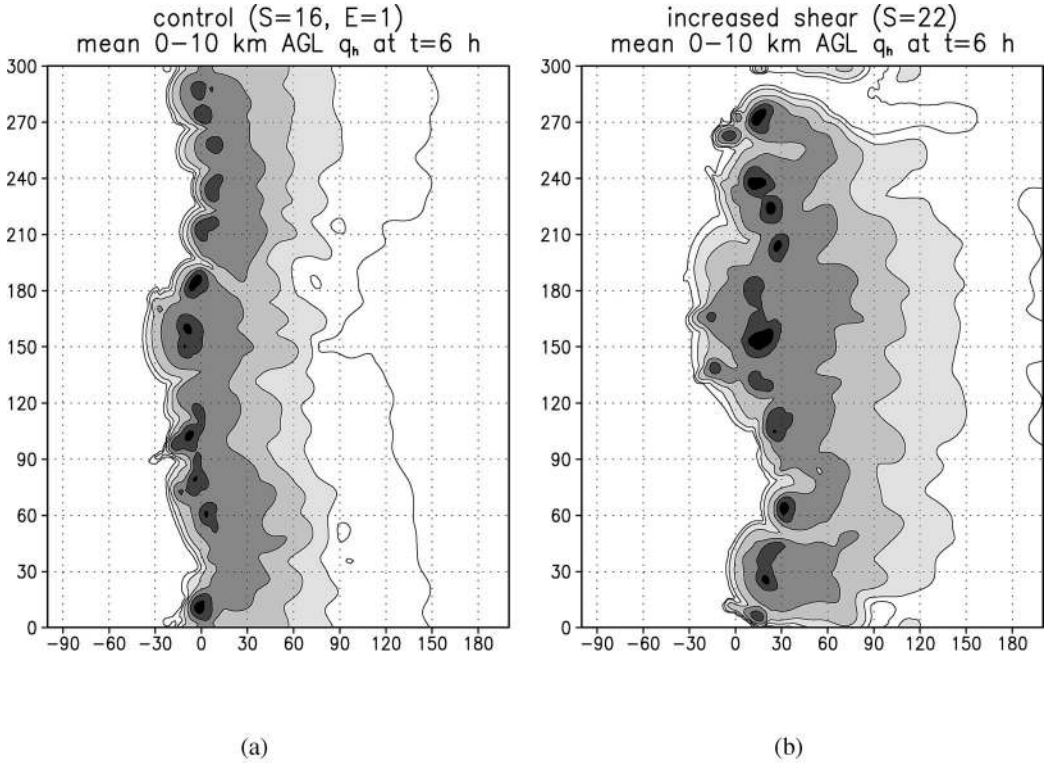

FIG. 6. Mean hydrometeor mixing ratio from 0–10 km AGL at 6 h for periodic-3D simulations: (a) control ($S=16$) simulation; (b) increased 3–10-km shear ($S=22$) simulation. Levels of shading are 0.005, 0.02, 0.08, 0.32, 1.28, and 5.12 g kg^{-1}.

7, on average over a period of approximately 75 min, the near-line sounding is cooler and moister than the environment below about 550 hPa (approximately 4.5 km AGL), with a lapse rate steeper than that of the environment in the lower troposphere. Although the full tropospheric convective available potential energy (CAPE) is decreased slightly (2517 J kg^{-1} versus 2577 J kg^{-1} in the environment) owing to warming aloft, CIN is also diminished (-24 J kg^{-1} versus -34 J kg^{-1}), and the 0–3-km CAPE is nearly doubled (198 J kg^{-1} versus 103 J kg^{-1}), which is to say that healthy updrafts can be easily triggered in the lower troposphere by the simulated system. Indeed, in some cases the near-line soundings even exhibit moist absolute instability (Bryan and Fritsch 2000). In the ensuing discussion, at any position an air parcel's potential temperature perturbation (θ') is the deviation from the base state θ at that height; therefore, columns in which θ' decreases with height have been destabilized with respect to the environment.

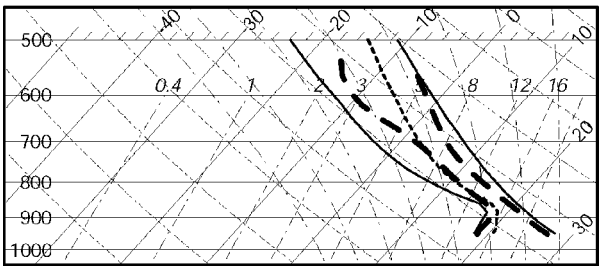

FIG. 7. Skew T–ln$p$ diagram of the lower troposphere for base-state initial condition (thin solid), wet-bulb temperature of base state (medium weight dotted), and mean near-line sounding (heavy dashed) for mature stage of $S=16$, $E=1$ (control) simulation, averaged from 2 h 40 min–3 h 55 min. Values of θ' for the near-line sounding are given in the right-hand column of Table 7a. The full depth of the base-state sounding is shown in Fig. 3 of Part I.

Three mechanisms for destabilizing the near-line sounding suggest themselves. 1) Because θ increases with height in the base state, air that ascends and conserves its potential temperature will be cooler than the environment; in a large region of dry ascent, the lapse rate will thereby tend toward the adiabatic value. In addition, because θ_e decreases with height in the base state (i.e., it is potentially unstable), lifting the layer to saturation will also destabilize it. 2) Because θ_e decreases with height, the layer could be destabilized by evaporatively cooling it to saturation. The base state's profile of wet-bulb temperature in Fig. 7 reveals that evaporatively cooling the lower troposphere to saturation would increase the temperature lapse rate in the layer from approximately 880–700 hPa (approximately 600–2600 m AGL). Additionally, as is clear from Fig. 7, the lowest 50–70 hPa of the sounding were not chilled

as much as the layer between about 880 and 700 hPa, such that the low levels were also destabilized somewhat. 3) Because the minimum in θ' is quite close to the 0°C level (about 620 hPa or 3400 m AGL, see Fig. 7), it is likely that chilling owing to the melting of falling snow and graupel is maximized aloft near the melting level, further increasing the lapse rate. Such destabilization by melting has been known at least since Findeisen (1940), as reviewed by Heffernan and Marwitz (1996). The following text discusses these three mechanisms in turn.

Temporally averaged wind trajectories (i.e., streamlines) do indeed reveal that the inflowing air in the lower troposphere ascends on its way to the convective line (Fig. 8). Because the base state is stable ($d\theta/dz > 0$), adiabatic ascent implies local perturbations in θ, following:

$$\frac{D\theta'}{Dt} = \frac{D\theta}{Dt} - \frac{D\theta_o}{Dt} = \dot{Q}_{\text{diabatic}} - w\frac{d\theta_o}{dz}. \qquad (8)$$

On average, inflowing air ascends over the lowest 1.5 km AGL in the 2D simulation and over the lowest 2.5 km AGL in the periodic 3D simulation (Fig. 8). In the 2D case, as the laterally moving parcels above 2 km AGL acquire hydrometeor loading and are chilled by melting and evaporation, they begin to descend (west of $x = 20$–25 km in Fig. 8a). In this region, the warming due to subsidence roughly offsets the chilling from phase changes, as evident by the small gradient in θ' along the upper trajectories in Fig. 8a. This subsidence mechanism is not prominent in the 3D case owing to the decreased mean hydrometeor content in the line-leading region (Fig. 8b). Table 7 summarizes each term in (8) integrated over the length of the inflow trajectories in Fig. 8; the total destabilization of the near-line column can be inferred from the vertical profile of the final potential temperature perturbations of its constituent air parcels (θ'_f in Table 7). For the 2D mean flow trajectories (Table 7a), perturbations owing to vertical displacement ($-\Delta\theta_o$ over the length of the trajectory) accounted for 50% or less of the total cooling along each trajectory. In contrast, ascent was quite important to the negative temperature perturbations along mean trajectories from the periodic 3D simulation (Table 7b), accounting for as much as 110% of the change in θ'. Notably, many of the trajectories began with significant θ', which was partly due to ascent and was partly due to the fact that the trajectories above 1.5 km AGL began within the leading precipitation and had already been chilled by evaporation and melting (Fig. 8).

As shown in Fig. 9, the upward accelerations causing ascent within and ahead of the leading precipitation region are primarily attributable to the ACCB imposed by the vertical gradient in p'_B. The p'_B field owes its existence to the surface cold pool, which is west of the domain depicted in Fig. 9, and to the region of strong negative buoyancy centered around 2200 m AGL within the leading precipitation region (Fig. 9), which exists in part because of persistent evaporation and melting in the region. Therefore, although ascent accounts for a significant part of the cooling along air parcel's trajectories, it is proper to say that the presence of the preline precipitation favors this ascent because the chilling that it induces yields a buoyant pressure field that is favorable for upward accelerations as air parcels flow into the leading precipitation region.

In addition, despite the fact that there is ascent on average in the preline region, many individual air par-

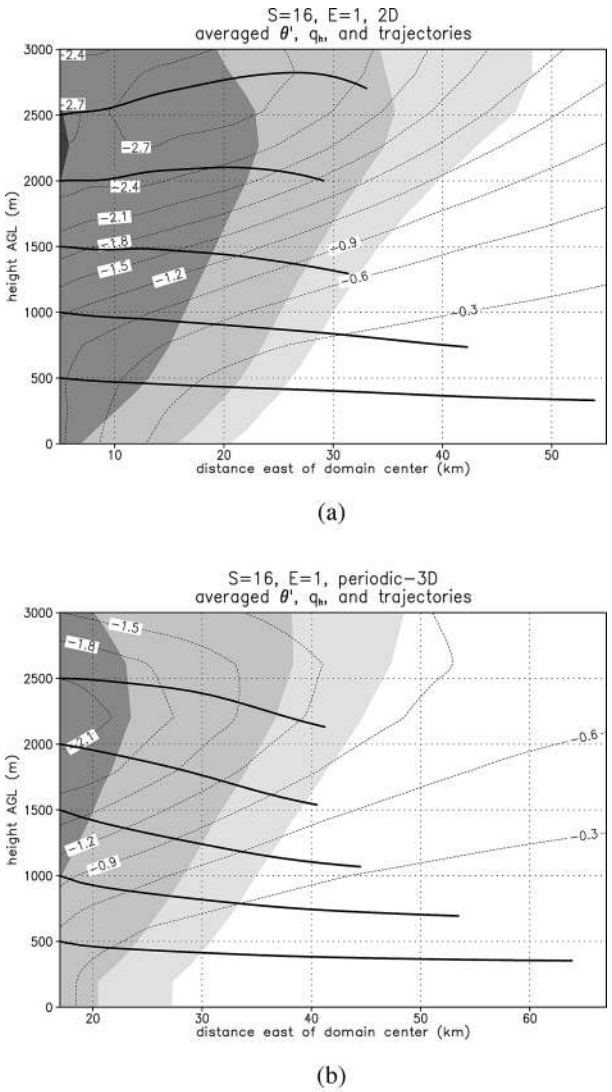

FIG. 8. Mean hydrometeor mixing ratio (shaded), potential temperature perturbation (contoured, interval = 0.3 K), and trajectories for $S=16$, $E=1$ (control) simulations: (a) for 2D simulation, averaged from 2 h 40 min to 3 h 55 min; (b) for periodic-3D simulation, averaged in $\hat{y}$ and from 5 h to 6 h 10 min. Levels of shading are 0.005, 0.02, 0.08, and 0.32 g kg^{-1}, and are the same in both (a) and (b). The trajectories follow the mean flow throughout the time intervals for each case. Data for the plotted trajectories are given in Table 7a,b.

TABLE 7. Data for trajectories that compose destabilized near-line soundings in $S=16$, $E=1$ (control), 2D, and periodic-3D simulations. (a) Trajectories computed for the mean flow field for 2D simulation, averaged from 2 h 40 min to 3 h 55 min (cf. Fig. 8a). (b) Trajectories computed for the mean flow field for periodic-3D simulation, averaged in $\hat{y}$ and from 5 h to 6 h 10 min (cf. Fig. 8b). (c) Forward trajectories computed in the evolving flow field of periodic-3D simulation (cf. Fig. 10). The data columns are z_i (m), the initial parcel height; z_f (m), the final parcel height; $\Delta\theta'$ (K), the change in the potential temperature perturbation over the trajectory's duration; $-\Delta\theta_o$ (K), the change in the potential temperature perturbation attributable to ascent over the trajectory's duration; $\Sigma\,(\dot{\theta}_M + \dot{\theta}_E)$ (K), the change in the potential temperature perturbation attributable to evaporation and melting over the trajectory's duration; and θ'_f (K), the parcel's final potential temperature perturbation with respect to the base state.

	Trajectories	z_i	z_f	$\Delta\theta'$	$-\Delta\theta_o$	$\Sigma\,(\dot{\theta}_M + \dot{\theta}_E)$	θ'_f
a)	2D	331	500	−0.9	−0.2	−0.7	−0.9
	Mean	736	1000	−1.0	−0.5	−0.6	−1.2
	2 h 40 min–3 h 55 min	1295	1500	−1.2	−0.5	−0.8	−1.9
		2001	2000	−1.2	+0.0	−0.8	−2.5
		2703	2500	−0.4	+0.6	−1.0	−2.7
b)	Periodic 3D	354	500	−0.5	−0.1	−0.4	−0.6
	Mean	694	1000	−0.9	−0.5	−0.4	−1.0
	5 h–6 h 10 min	1069	1500	−1.3	−0.9	−0.4	−1.6
		1539	2000	−1.4	−1.2	−0.2	−2.1
		2131	2500	−1.0	−1.1	+0.1	−2.1
c)	Periodic 3D	200	300	−1.1	−0.1	−1.0	−1.1
	Evolving flow	1000	1204	−1.9	−0.4	−1.5	−1.9
	0 h–3 h	1400	1417	−2.1	−0.0	−2.1	−2.1
		2202	2301	−2.7	−0.3	−2.4	−2.7
		3021	2893	−2.0	+0.4	−2.4	−2.0

cels in the temporally evolving flow field do not faithfully follow the mean-state streamlines in Fig. 8. An example of this is depicted in Fig. 10, in which a set of inflowing air parcels that compose a destabilized near-line sounding in the periodic 3D simulation have scarcely ascended at all (see their actual displacements in Table 7c). As shown in Table 7c, the cooling that occurs along these time-dependent trajectories is significant, and is almost entirely attributable to evaporation and melting. Hence, the contribution from evaporation and melting is not only important on average, but is predominant in some examples.

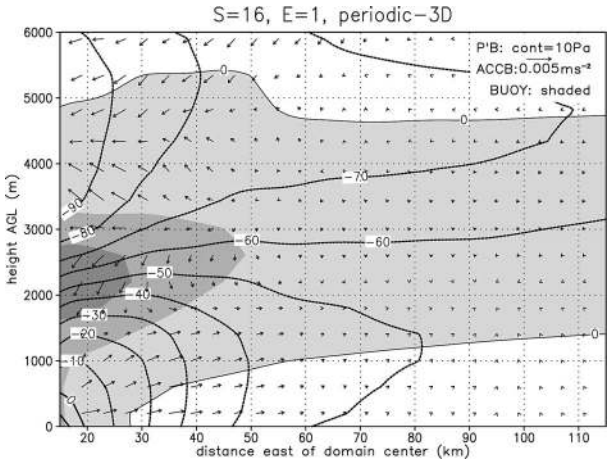

FIG. 9. Buoyant components of the acceleration and pressure fields for $S=16$, $E=1$ (control), periodic-3D simulation, averaged in $\hat{y}$ and from 5 h to 6 h 10 min. BUOY is shaded with levels: −0.04, −0.02, and 0 m s^{-2} (white/unshaded values are positively buoyant); p'_B is shown by heavy contours; ACCB is shown by vectors. See Fig. 8 for mean air parcel trajectories and distribution of hydrometeors.

The mean hydrometeor mass field in Fig. 8a is almost entirely composed of rain and graupel (Fig. 11). In the modeled system graupel predominates above the melting level, which is just above 3 km AGL (Fig. 11b), whereas rain predominates below about 2.5 km AGL (Fig. 11a). Between 2.5 and 3 km AGL there is a zone in which much of the falling graupel melts (Fig. 11). Both melting of graupel and evaporation of rain contribute significantly to the chilling such that, for the lower-tropospheric part of the leading precipitation region, (8) can more appropriately be written

$$\frac{D\theta'}{Dt} \approx \left(\frac{D\theta}{Dt}\right)_{\text{melting}} + \left(\frac{D\theta}{Dt}\right)_{\text{evaporation}} - w\frac{d\theta_o}{dz}. \quad (9)$$

In nature, snow aggregates are probably present in significant concentrations near the melting level, and could play a vital part in the melting budget. In the present simulations [using a Lin et al. (1983)–type parameterization], snow is advected forward quasi-horizontally from the convective line and composes the leading anvil aloft. As snow particles in this region settle downward and aggregate, they are ''autoconverted'' into the graupel category. In this respect, the graupel category is an alias for precipitation-sized ice with appreciable fall speeds in the leading precipitation region. Therefore, although snow probably contributes nontrivially to the melting budget in nature, it does not in the model simulations. However, given snow particles' small fall speeds, even if significant snow existed near the melting level it would likely be advected back toward the convective line by the lower- and middle-tropospheric flow, such that the zone of significant melting/cooling would not extend much farther ahead of the line.

Cooling that increases with height destabilizes the

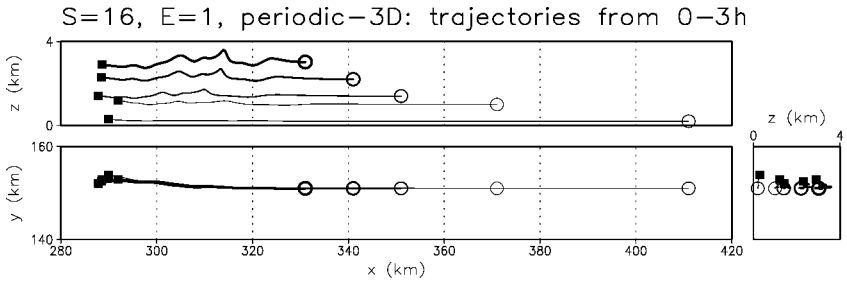

FIG. 10. ''Shadow'' depiction of forward trajectories computed in the evolving flow field of $S=16$, $E=1$ (control), periodic-3D simulation. These are ''best match'' forward trajectories that approximately compose a near-line sounding at $t = 3$ h. Data points for this near-line sounding are shown in Table 7c. The central panel of this figure is an x–y plane view of trajectory positions, the top panel is an x–z cross section of trajectory positions, and the right panel is a z–y cross section of positions. The trajectories begin at the ○ symbols and end at the ■ symbols. The trajectories' thicknesses vary in order to assist in differentiating them. The thicknesses have no other meaning.

near-line sounding and, as seen in Fig. 12, all three components contribute significantly to destabilization in some part of the 2D simulation's leading precipitation region. In the 2D simulation the near-line environment is characterized by evaporation, melting, and subsident warming (Fig. 12). To some degree, this may therefore resemble the subsidence and corresponding sublimation, melting, and evaporation in the *transition zone* of FFTS systems, as discussed, for example, by Biggerstaff and Houze (1991). Although the magnitude of the melting source is somewhat smaller than those associated with evaporation or ascent (mostly owing to the fact that the latent heat of melting is much less than that of vaporization), it provides chilling that is maximized aloft (Fig. 12c), that is, just where it is needed to destabilize the lower troposphere. The melting, in tandem with the evaporation (Fig. 12b), contributes to a profile of chilling that increases with height from about 1 to 2.5 km AGL, even though the subsidence that results offsets it to some degree. Notably, Fig. 12b implies that the lowest 1 km of the inflow layer ought to be stabilized by decreasing evaporation with height near the convective line. The detrimental effect of this process is minimized because the inflow in the lowest 1 km AGL is moving westward rapidly, and therefore does not spend much time in the region of significant chilling.

In all three examples the cooling along the trajectories increases with height over the lowest 2 km AGL (Table 7). For the 2D simulation (Table 7a), in which a relatively small amount of destabilization happens along the trajectories, neither ascent nor phase changes are clearly the predominant contributor to the destabilized ($\partial\theta'/\partial z < 0$) near-line sounding. On average, in the periodic-3D simulation (Table 7b), ascent is the predominant contributor to destabilization. For the group of time-dependent trajectories from the periodic-3D simulation (Fig. 10 and Table 7c), evaporation and melting are the predominant contributors to destabilization.

The destablizing effects of ascent and of melting aloft are relatively straightforward. Additionally, evaporation throughout a layer can destabilize it provided that the cooling rate increases with height. When θ_e decreases with height the possibility exists for a layer to become absolutely unstable when saturated by local evaporation. As shown in Fig. 7, in the present study the relative humidity of the base state decreases with height above the surface mixed layer. In addition to this, the rainwater mixing ratio generally increases with height in the lowest 2 km AGL of the leading precipitation region (Fig. 11a). This is partly because the precipitation evaporates as it falls from above, and partly because the front-to-rear storm-relative flow advects hydrometeors back toward the convective line as they fall through the lower troposphere. Finally, because the storm-relative wind speeds decrease with height, air parcels at higher altitudes spend more time within the leading precipitation, and hence have longer to be chilled. These four factors together mean that inflowing air can be cooled to lower temperatures with increasing height, and that the evaporative chilling profile will increase with height because the relative humidity of the inflowing air decreases with height, q_h increases with height, and the Lagrangian time scale increases with height.

In summary, leading precipitation provides two beneficial effects, both of which tend to destabilize the near-line sounding. The leading precipitation does cool the inflowing air, as PJ00 originally speculated, but it does so in a way that is not detrimental to the system's longevity. First, the leading precipitation melts and evaporates as it falls into the inflow, rendering cooling that increases with height over the lowest 2–2.5 km AGL. Notably, this sort of destabilization bears some resemblance to the removal of a capping inversion by virga, as discussed by Tripoli and Cotton (1989). Second, as widespread evaporation and melting ensue, they lead to a pressure field that induces upward acceleration on inflowing air parcels in and ahead of the leading precip-

itation region. Fovell (2002) has described in similar terms the effects that FFTS systems can have on their downshear environments. Because in the present FFLS simulations, θ_e decreases with height in the lower troposphere, and because the air parcels' vertical displacements often increase with height, this process also destabilizes the near-line profile as the cooled inflowing air parcels arrive there. Therefore, the leading precipitation region helps to foster continued development of healthy convection because the destabilization that it provides overwhelms any stabilization from gravity wave–induced subsidence.

b. Sensitivity to microphysics scheme

One difficulty of the microphysics scheme in this study is that it must represent both the dense hailstones in the modeled convective region, as well as the less dense graupel in the stratiform region [Rutledge and Houze (1987) suggested $\rho_g = 0.3$ g cm^{-3} as appropriate for the stratiform region of an MCS]. We performed several sensitivity tests, summarized in Table 1, designed to determine how the settings of the model's ice microphysics scheme might impact the general evolution of the simulated FFLS systems, as well as the destabilization mechanism in this section. In the Lin et al. (1983) scheme, the terminal velocities of the graupel particles are given by

$$v_{tg} = \left(\frac{4g\rho_g D}{3C_d\rho_a}\right)^{0.5}, \tag{10}$$

wherein C_d is a drag coefficient. Accordingly, in the parameterization as in nature, the fall speeds of graupel particles of a given size decrease as ρ_g is decreased. Additionally, in the scheme of Lin et al. [1983, see their Eq. (47)], the graupel melting rate is a complicated function that decreases with increasing ρ_g; in nature this is attributable to the decreased surface area per unit mass. As a result, in simulations with lower ρ_g, ice particles have more time to fall and melt more rapidly during that time. This contributes to increased chilling from melting. Additionally, as noted by Gilmore et al. (2002), growth rates for the graupel category increase when ρ_g is decreased, which provides more available ice mass in the graupel category for melting. Finally, because the lower-density particles melt more completely at higher altitudes, there is more liquid water available in the lower levels for evaporation (and chilling).

Surprisingly, this has a relatively small effect on the destabilization mechanism described in section 4a; the along-line-averaged temperature perturbations at 2.2 km AGL were only increased by about 10% in the ρ4 simulation compared to the control run. In the ρ4 case, the region of chilling was also slightly broader in across-line extent, but this did not appear to have a significant effect. This insensitivity may exist, in part, because the graupel mixing ratios are relatively small in the preline region. However, decreasing ρ_g has a significant effect on the generation of the surface cold pool by the convective cells. The maximum chilling rates owing to melting graupel in the convective cores of the ρ4 run were increased by nearly 40% over the control run (not shown) owing to the particles' smaller fall speeds and greater melting rates. Therefore, although the settings in the ice microphysics scheme do not appear to greatly impact the destabilization and maintenance mechanism described in this section, they do significantly impact the evolution toward FFTS structure owing to their role in increasing the strength of the surface outflow. The ρ4 simulation acquired TS structure almost twice as rapidly as the control simulation in 2D. However, once

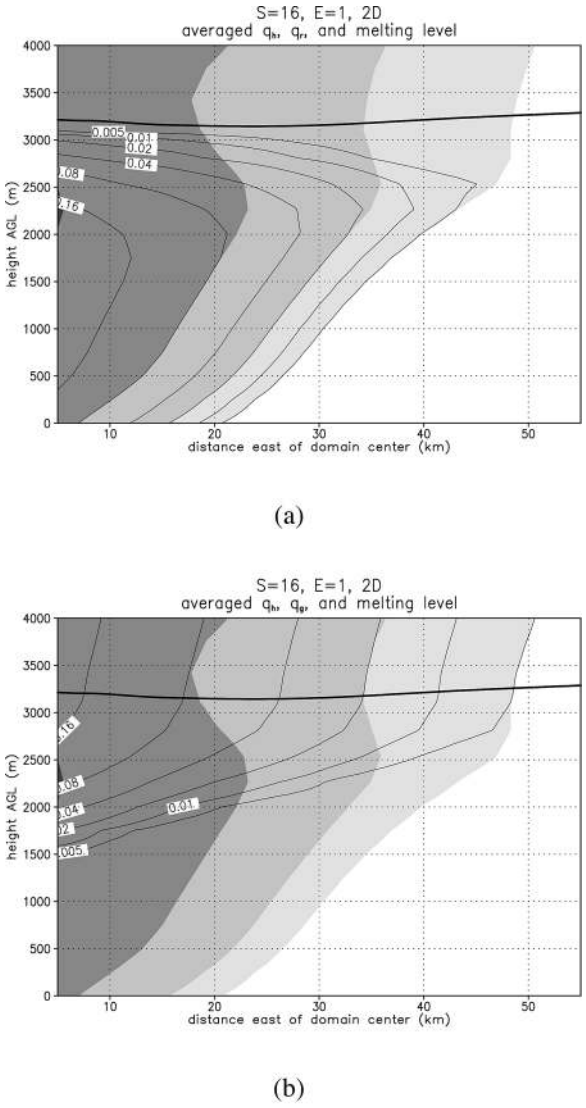

FIG. 11. Mean hydrometeor mixing ratio (levels of shading are 0.005, 0.02, 0.08, and 0.32 g kg^{-1}) and 0°C isotherm (bold contour) for control 2D simulation, averaged from 2 h 40 min to 3 h 55 min, along with (a) rain mixing ratio (light contours, g kg^{-1}) and (b) graupel mixing ratio (light contours, g kg^{-1}).

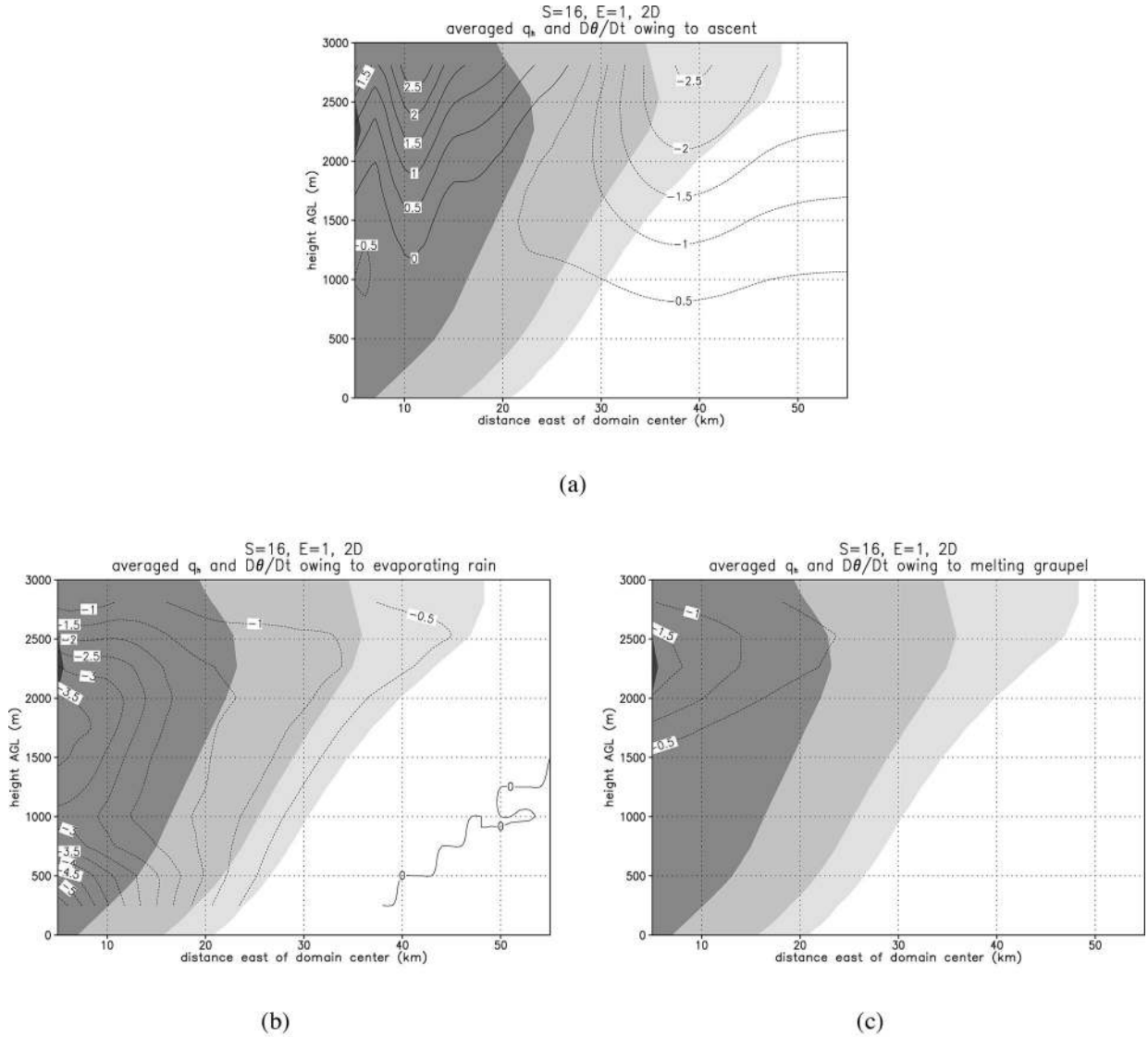

FIG. 12. Mean hydrometeor mixing ratio (levels of shading are 0.005, 0.02, 0.08, and 0.32 g kg^{-1}) for control 2D simulation, averaged from 2 h 40 min to 3 h 55 min, along with (a) warming/cooling rate owing to mean descent/ascent (contours, K h^{-1}), (b) heating/chilling rate owing to evaporation of falling rain (contours, K h^{-1}), and (c) heating/chilling rate owing to melting of falling graupel (contours, K h^{-1}). The curves are truncated at the upper and lower edges because the computation involved a vertical derivative.

again, as in section 3, the 3D simulations were more resistant to the FFLS–FFTS evolution than were the 2D simulations. Indeed, in 3D the $\rho 4$ simulation was qualitatively very similar to the control simulation, and did not evolve toward TS structure during the 6 h simulated (not shown).

The sensitivity tests in which n_{og} varied ($n10^{-3}$ and $n10^{-5}$ in Table 1) generally showed even less dramatic changes, much as discussed by Gilmore et al. (2002). In general, their effects could be inferred from consideration of the mean particle fall speeds. When n_{og} was increased, as in $n10^{-3}$, fewer large particles were present, the distribution's mean fall speed was decreased, and evolution toward TS structure was hastened owing to the previously described mechanism. When n_{og} was decreased, as in $n10^{-5}$, the evolution toward TS structure was correspondingly postponed. As with changes in ρ_g, changes to n_{og} had a small effect on the preline destabilization mechanism. Sensitivity tests using the Schultz (1995) scheme evolved to TS structure more rapidly, but the destabilization of the LS region again did not change very much (not shown). Sensitivity tests in which we used the Kessler (1969) warm rain scheme were considerably different owing to the absence of the ice phase; destabilization still occurred, but it was attributable solely to ascent and evaporation, and was dis-

tributed over a deeper vertical layer owing to the presence of liquid water higher in the model troposphere (not shown).

Another factor to which the destabilization mechanism is presumably sensitive is the humidity above the moist well-mixed boundary layer. In sensitivity tests with increased middle-tropospheric humidity (increased from a minimal value of 0.35 to 0.5), there was slightly less destablization of the leading precipitation region (the mean temperature perturbation at 2.2 km AGL was about 15% smaller). In sensitivity tests with decreased middle-tropospheric humidity (decreased from a minimal value of 0.35 to 0.2), there was more destablization of the leading precipitation region (the mean temperature perturbation at 2.2 km AGL was about 25% greater). Hence, *one irony of the FFLS structure is that, although dry air in the middle troposphere is generally detrimental to convection on short time scales owing to entrainment, it can be helpful to a long-lived FFLS system because it enhances the destabilization mechanism that takes place in the leading precipitation region.*

5. Synthesis

Simulated 2D and periodic-3D convective lines with LS precipitation can be quasi-stable and long lived, much as are their real-world counterparts. The structure of FFLS systems is predominated by a front-to-rear lower-tropospheric flow stream that passes through the LS region and feeds an overturning updraft, which in turn gives rise to the region of line-leading precipitation. As in section 4 of Part II, a prime reason that these systems can be long lived, despite the seemingly detrimental effects of water loading and evaporation upon their inflow, is a destabilization mechanism that occurs in the lower to middle troposphere in the LS region. In the present simulations melting and evaporation, owing to the cascade of preline hydrometeors into the inflow, are maximized between 1.5 and 2.5 km AGL and thereby increase the near-line lapse rate. As well, the pressure field that results from this vertical profile of cooling induces ascent in the inflowing airstream, which further contributes to the destabilization. Hence, the presence of preline precipitation can actually benefit a convective system by increasing the conditional instability of the base state. This result appears to be fairly robust, although the vertical profile of humidity does have an effect on it.

The analyses in Part I showed that the accelerations that cause updraft air parcel trajectories to overturn (and feed the LS region) are transient, and are lost when the model output is averaged over periods of time approaching the multicellular period. The fundamental dynamics that account for the downshear acceleration of the updraft parcels incorporate nontrivial contributions from both the linear and nonlinear parts of the dynamic pressure field (ACCDL and ACCDNL), as well as the buoyant pressure field (ACCB). The overturning updraft parcels carry their total water content with them into the leading precipitation region, and it is the cascade of heavy convective precipitation into the inflowing air stream that apparently cuts off the convective cell from the inflow and determines the multicellular period. As described in Part I, because the sign and magnitude of ACCDL in the middle troposphere leads to positive feedbacks in both ACCB and ACCDNL in a mature FFLS system, the simulated FFLS structures are sensitive not only to the lower-tropopsheric cold pool–shear balance (as in Rotunno et al. 1988), but also to the middle-tropospheric shear.

Notwithstanding the importance of the transient accelerations to the evolving structure of the FFLS system, the temporally averaged flow fields are also of interest. By maturity, simulated FFLS systems have perturbed the mesoscale pressure field in such a way that, on their line-leading sides, a persistent midlevel front-to-rear flow jet is accelerated, whereas the lower-tropopsheric inflowing airstream is decelerated. The decreased vertical wind shear that attends these perturbations in the preline region ultimately contributes to increasingly rearward-sloped updrafts in time, which are attributable to continual decreases in the downshear-directed dynamic pressure gradient accelerations of the updraft parcels. This gradual evolution toward more rearward-tilting updrafts can reach a critical point, beyond which the cold pool's strength, the convection's rearward tilt, and the pressure field beneath and behind the convective line may feed back on one another.

This suggests that FFLS systems are somewhat enigmatic features of the mesoscale. FFLS systems assist in their own longevity by producing preline precipitation, which destabilizes the inflowing airstream, particularly in relatively dry environments that might otherwise hinder long-lived convection. However, this very same FFLS structure also locally disrupts its own inflowing airstream on the convective time scale, as precipitation cuts each updraft off during the multicell cycle. More importantly, the environmental wind modifications produced by a mature FFLS system hasten its demise, or its transition away from FFLS structure and toward FFTS structure, because they decrease the local vertical wind shear as time goes on. It seems plausible that this process may limit the lifespan of the archetypal FFLS structure of MCSs in the real world, which are generally shorter lived than TS systems according to PJ00. Notably, however, the simulated periodic-3D systems were more resistant to this evolution, and the present work suggests that the FFLS archetype may stand on the margin of the convective systems that can be reasonably simulated in 2D. Indeed, the simulated 3D systems begin to take on supercellular characteristics in environments with only slightly more wind shear.

6. Indicated future work

As with any numerical study, it is desirable to verify the present conclusions with observational data; the au-

thors sincerely hope that more research-quality data (e.g., dual-Doppler radar measurements) on FFLS systems will be collected in the near future, whether by means of a field campaign or by development of new instruments that are well suited to the problem. In the mean time, additional numerical studies of FFLS MCSs and other nonclassical convective systems may bear fruit, particularly if they can faithfully represent increased complexity by more actively incorporating line-end effects, Coriolis accelerations, radiation, and surface fluxes, as well as more sophisticated initial conditions. It is also interesting to note that both the simulated systems and Liu and Moncrieff's (1996) analytical models for a density current in shear include layers of front-to-rear low-level flow, midlevel overturning updrafts, and in the 2D case, upstream stagnation in the middle and upper troposphere, making them perhaps the only convective phenomena to possess such a structure (M. Moncrieff 2002, personal communication). Such models might depict the net impacts of an FFLS system upon its environment, suggesting that analytical solutions could provide additional insight into the dynamics of the mean FFLS structures. Finally, as discussed in section 4, the FFLS convective regime appears to border or overlap the supercellular regime. A fuller understanding of the FFLS–supercell continuum would be of interest to forecasters and warning meteorologists, who often must make decisions between tornado and severe thunderstorm watches and warnings based upon sparse data.

7. Conclusions

The authors utilized the Advanced Regional Prediction System (ARPS) to simulate convective lines with leading precipitation. This paper, along with Part I, constitutes perhaps the first thorough examination of front-fed convective lines with leading stratiform precipitation (FFLS systems). In section 5 of this article, the authors presented a consolidated depiction of the structures, governing dynamics, and mechanisms for maintenance and evolution of idealized, simulated FFLS systems, synthesizing and reviewing the results from both Parts I and II. This second paper specifically focused on the following chief results.

In addition to the well-known balance between the low-level shear and surface cold pool, the middle- and upper-tropospheric wind shear are also important to the updraft tilt and overall structure of FFLS systems. The perturbed pressure fields associated with mature FFLS systems tend to decrease the vertical wind shear in the preline region, which appears to gradually contribute to more rearward-sloping updrafts and may hasten a positive feedback mechanism that causes a transition toward a convective line with trailing precipitation structure. However, simulated 3D systems do not evolve so readily, suggesting that the FFLS structure can be somewhat robust in the real world. Indeed, sensitivity tests show that FFLS systems may represent the high-shear limit of the quasi-2D regime.

Importantly, inflow that passes through a curtain of stratiform precipitation need not be detrimental to the convection that it feeds. In the simulations, inflowing air was destabilized by lifting and by the vertical profile of evaporation and melting as it passed through the line-leading precipitation region. This process helped to maintain the simulated FFLS systems, and was relatively unaffected by changes to the model's microphysics parameterization. Hence, FFLS systems are somewhat enigmatic in that they provide a means for their own sustenance owing to their preline destabilization process, but also provide a means for their own demise owing to their tendency to decrease the lower-tropospheric wind shear.

In the coming years, the authors hope that high-quality data will be collected, with which to advance our basic knowledge of FFLS systems as well as other nontraditional MCSs. Such systems are common in the agriculturally vital Great Plains, and can impact society by producing severe weather and flooding rains.

Acknowledgments. The authors gratefully acknowledge the suggestions and contributions of M. Moncrieff and M. Weisman of the National Center for Atmospheric Research (NCAR), R. Fovell of UCLA, W. Cotton and S. Rutledge of Colorado State University (CSU), and R. Maddox of Tucson, AZ, as well as the assistance of J. Knievel of CSU and NCAR, S. Tulich of CSU, and Z. Eitzen of CSU and the National Aeronautics and Space Administration. We also thank G. Cordova and R. Taft of CSU for their help throughout this work. The simulations in this study were made using the Advanced Regional Prediction System (ARPS) developed by the Center for Analysis and Prediction of Storms (CAPS), University of Oklahoma. CAPS is supported by the National Science Foundation (NSF) and the Federal Aviation Administration through combined Grant ATM92-20009. NCAR provided supercomputer facilities and computational time for many of the simulations in this study, and D. Valent of NCAR's Scientific Computing Division was instrumental in helping us to exploit these resources. NSF funded this research under Grant ATM-0071371.

REFERENCES

Biggerstaff, M. I., and R. A. Houze Jr., 1991: Kinematic and precipitation structure of the 10–11 June 1985 squall line. *Mon. Wea. Rev.,* **119,** 3034–3065.

Bryan, G. H., and M. J. Fritsch, 2000: Moist absolute instability: The sixth static stability state. *Bull. Amer. Meteor. Soc.,* **81,** 1207–1230.

Charba, J., 1974: Application of gravity current model to analysis of squall-line gust front. *Mon. Wea. Rev.,* **102,** 140–156.

Dudhia, J., M. W. Moncrieff, and D. W. K. So, 1987: The two-dimensional of West African squall lines. *Quart. J. Roy. Meteor. Soc.,* **113,** 121–146.

Findeisen, W., 1940: The formation of the 0°C-isothermal layer and fractocumulus under nimbostratus. *Meteor. Z.,* **76,** 49–54.

Fovell, R. G., 2002: Upstream influence of numerically simulated squall-line storms. *Quart. J. Roy. Meteor. Soc.,* **128,** 893–912.

Gilmore, M. S., J. M. Straka, and E. N. Rasmussen, 2002: Quantitative precipitation in simulated deep convection: Sensitivity to the hail/graupel category. Preprints, *15th Conf. on Numerical Weather Prediction,* San Antonio, TX, Amer. Meteor. Soc., 139–142.

Grady, R. L., and J. Verlinde, 1997: Triple-Doppler analysis of a discretely propagating, long-lived, High Plains squall line. *J. Atmos. Sci.,* **54,** 2729–2748.

Hane, C. E., 1973: The squall line thunderstorm: Numerical experimentation. *J. Atmos. Sci.,* **30,** 1672–1690.

Heffernan, E., and J. Marwitz, 1996: The Front Range blizzard of 1990. Part II: Melting effects in a convective band. *Mon. Wea. Rev.,* **124,** 2469–2482.

Kessler, E., 1969: *On the Distribution and Continuity of Water Substance in Atmospheric Circulations. Meteor. Monogr.,* No. 32, Amer. Meteor. Soc., 84 pp.

Lin, Y.-L., R. D. Farley, and H. D. Orville, 1983: Bulk parameterization of the snow field in a cloud model. *J. Climate Appl. Meteor.,* **22,** 1065–1092.

Liu, C., and M. W. Moncrieff, 1996: A numerical study of the effects of ambient flow and shear on density currents. *Mon. Wea. Rev.,* **124,** 2282–2303.

Nicholls, M. E., R. H. Johnson, and W. R. Cotton, 1988: The sensitivity of two-dimensional simulations of tropical squall lines to environmental profiles. *J. Atmos. Sci.,* **45,** 3625–3649.

Orlanski, I., 1975: A rational subdivision of scales for atmospheric processes. *Bull. Amer. Meteor. Soc.,* **56,** 527–530.

Parker, M. D., and R. H. Johnson, 2000: Organizational modes of midlatitude mesoscale convective systems. *Mon. Wea. Rev.,* **128,** 3413–3436.

——, and ——, 2004a: Simulated convective lines with leading precipitation. Part I: Governing dynamics. *J. Atmos. Sci.,* **61,** 1637–1655.

——, and ——, 2004b: Structures and dynamics of quasi-2D mesoscale convective systems. *J. Atmos. Sci.,* **61,** 545–567.

Rotunno, R., J. B. Klemp, and M. L. Weisman, 1988: A theory for strong, long-lived squall lines. *J. Atmos. Sci.,* **45,** 463–485.

Rutledge, S. A., and R. A. Houze Jr., 1987: A diagnostic modeling study of the trailing stratiform region of a midlatitude squall line. *J. Atmos. Sci.,* **44,** 2640–2656.

Schultz, P., 1995: An explicit cloud physics parameterization for operational numerical weather prediction. *Mon. Wea. Rev.,* **123,** 3331–3343.

Seitter, K. L., and H.-L. Kuo, 1983: The dynamical structure of squall-line type thunderstorms. *J. Atmos. Sci.,* **40,** 2831–2854.

Szeto, K. K., and H.-R. Cho, 1994: A numerical investigation of squall lines. Part II: The mechanics of evolution. *J. Atmos. Sci.,* **51,** 425–433.

Thorpe, A. J., M. J. Miller, and M. W. Moncrieff, 1982: Two-dimensional convection in non-constant shear: A model of midlatitude squall lines. *Quart. J. Roy. Meteor. Soc.,* **108,** 739–762.

Tripoli, G. J., and W. R. Cotton, 1989: Numerical study of an observed orogenic mesoscale convective system. Part 1: Simulated genesis and comparison with observations. *Mon. Wea. Rev.,* **117,** 273–304.

Weisman, M. L., J. B. Klemp, and R. Rotunno, 1988: Structure and evolution of numerically simulated squall lines. *J. Atmos. Sci.,* **45,** 1990–2013.

Xue, M., K. K. Droegemeier, V. Wong, A. Shapiro, and K. Brewster, 1995: *Advanced Regional Prediction System Version 4.0 Users Guide.* Center for the Analysis and Prediction of Storms, Norman, Oklahoma, 380 pp. [Available from ARPS Model Development Group, CAPS, University of Oklahoma, 100 East Boyd, Norman, OK 73019-0628.]

——, ——, and ——, 2000: The Advanced Regional Prediction System (ARPS)—A multiscale nonhydrostatic atmospheric simulation and prediction tool. Part I: Model dynamics and verification. *Meteor. Atmos. Phys.,* **75,** 161–193.

——, and Coauthors, 2001: The Advanced Regional Prediction System (ARPS)—A multiscale nonhydrostatic atmospheric simulation and prediction tool. Part II: Model physics and applications. *Meteor. Atmos. Phys.,* **76,** 134–165.